Unified biophysical mechanism for cell-shape oscillations and cell ingression

Wei-Chang Lo, Craig Madrak, Daniel P. Kiehart, and Glenn S. Edwards

Phys. Rev. E **97**, 062414 — Published 22 June 2018

DOI: 10.1103/PhysRevE.97.062414

Unified biophysical mechanism for cell-shape oscillations and cell ingression

Wei-Chang Lo,[1] Craig Madrak, [1] Daniel P. Kiehart, [2] and Glenn S. Edwards[1]

Physics[1] and Biology[2] Departments

Duke University, Durham NC 27708 USA

Abstract

We describe a mechanochemical and percolation cascade that augments myosin's regulatory network to tune cytoskeletal forces. Actomyosin forces collectively generate cytoskeletal forces during cell oscillations and ingression, which we quantify by elastic percolation of the internally-driven, cross-linked actin network. Contractile units can produce relatively large, oscillatory forces that disrupt crosslinks to reduce cytoskeletal forces. A (reverse) Hopf bifurcation switches contractile units to produce smaller, steady forces that enhance crosslinking and consequently boost cytoskeletal forces to promote ingression. We describe cell-shape changes and cell ingression in terms of inter-cellular force imbalances along common cell junctions.

Introduction

The cytoskeleton is an out-of-equilibrium structural network internally driven by actomyosin complexes (*1*). Actomyosin contraction is a ubiquitous source of molecular-force production that drives cell-shape changes, which collectively drive tissue movements to develop cell, tissue, organ, and organismal form during morphogenesis (*2*). Previous investigations of dorsal closure, a developmental stage of *Drosophila melanogaster* and a model system for cell-sheet morphogenesis (*3,4*), have characterized generic shape changes in amnioserosa cells that include oscillations in cross-sectional area transitioning to ingression (*5-7*). Ingression is the persistent loss of cross-sectional (apical) area as the cell internalizes below the remaining sheet of cells (amnioserosa tissue). Apoptosis is one of the ingression processes occurring during dorsal closure, which is characterized by relatively rapid ingression accompanied by an apoptotic force that provides one-third of the overall tissue force produced by the amnioserosa (*8*).

Cell oscillations have generated considerable interest (e.g., *9-14,6,7*). These oscillations occur at low-Reynolds number and from this perspective it was surprising

that a band of oscillation frequencies (5.7±0.9 mHz) was resolved in amnioserosa cells (*7*). Dierkes, *et al*., have put forth a compelling physical model that attributes these oscillations to nonlinear dynamics coupled with the turnover of contractile molecules (*13*); however, in this model each cell was abstracted as a 1-D, equivalent mechanical circuit. Inspired by the mathematical insights of the Dierkes model, we have investigated a molecular model for a 3-D cytoskeleton that: 1) identifies the key-attributes of a molecular contractile unit that leads to a unified mechanism for producing oscillations and the steady forces that promote ingression; 2) characterizes a regulatory process that switches contractile units from oscillatory to steady-force production; and 3) incorporates the role of actin cross-links in scaling piconewton actomyosin forces to nanonewton intercellular forces.

Results

The following subsections report results that range from molecular to cellular dynamics. We first present the molecular structure of contractile units, followed by quantifying their nonlinear elasticity and the turnover of their myosin mini-filaments. We find that oscillatory or steady forces arise at the level of these contractile units. Then we present the collective dynamics for boosting the piconewton contractile-unit forces into nanonewton cytoskeletal forces, which preserves the oscillatory or steady time dependence that arose at the molecular level. Furthermore, we quantify how the imbalance of intercellular forces on common cell junctions leads to either oscillations in the area of the apical cross-section or to the ingression of cells in tissue. We then quantitatively characterize a regulatory process for oscillatory contractile units switching into contractile units that produce steady forces with the consequence of cells exhibiting oscillations in apical cross-sectional area switching to ingressing cells within tissue. To validate this mechanochemical mechanism, we carry out numerical simulations that recapitulate experimental observations of oscillating amniosersosa cells switching to ingression during dorsal-closure.

Contractile unit: structure

We model the cytoskeleton as a network of actin filaments that form both myosin-independent cross-links and cross-bridges to myosin mini-filaments (Fig. 1). Cross-bridges produce mechanical forces and crosslinks transmit those forces through the actin

network. Recent high-resolution measurements using lattice-light sheet and TIRF-SIM microscopies find that the actin filaments are not disassembling and the actin network is not being compromised within the apicomedial cytoskeleton of the amnioserosa (15). The following defines a contractile unit that incorporates these key attributes (Fig. 1a) and summarizes biological evidence that is consistent with this definition. In particular, this subsection describes the structure of a contractile unit, its shape changes, and how it makes mechanical connections to distort its local cytoskeleton.

The structure of a contractile unit is shown schematically in Fig. 1a. A bi-polar myosin mini-filament is at the core of each contractile unit. Electron microscopy of *Drosophila* mini-filaments measured 14.9±3 heads at each end, which suggested that eight myosin-2 dimers assemble into a mini-filament comprising 16 monomers (*16*), where a myosin-2 monomer is a pair of myosin heavy chains, a pair of essential light chains, and a pair of regulatory light chains. Within a contractile unit, one end of the myosin mini-filament is cross-bridged to a segment of one actin filament and the other end is cross-bridged to a segment of another actin filament. Generally each of these two actin segments is cross-linked at two locations to filaments in the local (surrounding) actin network, where a segment is that fraction of an actin filament between its two cross-links (compare Fig. 1a and 1b). These four (myosin-independent) actin cross-links and these two actin segments lie at the periphery of this contractile unit (Fig. 1a). Each actin filament extends beyond its segment (beyond this contractile unit) to form part of the local actin network (Fig. 1b). Contractile unit forces are transmitted to the local cytoskeleton through these four crosslinks and the extensions of these two actin filaments. At very high concentrations myosin mini-filaments also can exhibit cross-linking behavior within an actin network (*17*) and Fig. 1b also includes two hybrid contractile units that could form at such high concentrations. For example, consider the contractile unit that includes the lower-right myosin mini-filament in Fig. 1b, where its upper actin segment is defined by an actin cross-link and by a cross-bridge attachment site to a neighboring myosin mini-filament. Its generic lower segment is defined by two cross-links.

Each contractile unit generates contractile (actomyosin) forces that can distort its local cross-linked actin network. The magnitude of these forces depends on the duty ratio

r, which is the fraction of time a myosin head is strongly bound to actin during the mechanoenzymatic cycle (*18*, page 222), and on the number N of heads that can bind actin. The filament duty ratio for one end of a myosin filament is $r_{filament} = 1 - (1 - r)^N$ (*19*). For *Drosophila* mini-filaments, the experimental value for r is 0.1 and $r_{filament}$ was calculated to be 0.81 (using N = 16) (*19*). The magnitude of the contractile force due to one end of a myosin mini-filament cross-bridged to an actin segment is $S\, r_{filament}\, F_{on}$, where $S \leq 1$ now takes into account steric constraints for forming cross-bridges and F_{on} is the average (piconewton) force exerted on the segment by a bound cross-bridge (*20*). Each contractile unit can transmit actomyosin forces along the four actin-filament extensions and through the four cross-links to distort the local cytoskeleton (Fig. 1b). The overall strain in the apicomedial cytoskeleton is due to the integrated stresses from numerous contractile units distributed throughout its cross-linked actin network (Fig. 1 e,f).

A contractile unit can change shape for two reasons. First, contractile-unit forces are generated at the actomyosin binding sites and transmitted along the segments to the cross-links. The local network also exerts external forces on these four cross-links at the periphery of each contractile unit. The net effect is the cross-link location and spacing can change as force balance is established. Second, the mechanism for generating the actomyosin forces also changes the geometry of the actin segments within the contractile unit. Actomyosin forces cause the myosin mini-filament to walk along each actin segment until stalling, which rotates the myosin mini-filament to drive the inward deflections of both elastic actin segments as portrayed in Fig. 1a,b. This cross-link geometry and segment orientation are consistent with the proposal by Verkhovsky and Borisy (*21*, figure 9). The conclusions that follow will generalize for other segment orientations.

Now we identify the direction of deflection that will be cited in the following. Consider the enumerated myosin mini-filament in Fig. 1b, reproduced in isolation in Fig. 1a. The deflected segment and the line connecting its two cross-links (two black dots) form a triangle, highlighted with shading in both panels. The height of this triangle is perpendicular to the dashed line connecting the two cross-links (Fig. 1c). The deflection direction lies along the height of this shaded triangle and the value of the height

satisfying force balance is the steady-state (or reference) deflection l_o. The steady-state forces for contraction $T(c_o,r)$ and elasticity $K(l_o)$ are anti-parallel and lie along the deflection direction. An analogous analysis can be applied to the lower shaded triangle.

Contractile unit: nonlinear elasticity

The dynamical equation for a contractile unit is based on Newton's Second Law at low-Reynolds number:

$$\mu\frac{dl}{dt} = T(c,r) - K(l) \quad \text{(Eq. 1)}$$

where $\mu\frac{dl}{dt}$ is the drag force and l is the deflection of an actin filament (the height of the triangle in Fig 1c). $T(c,r)$ is the component of the actomyosin forces relative to its steady-state value $T(c_o,r)$ and is given by the formula:

$$T(c,r) = T(c_o,r) + rt_1(c - c_o) \quad \text{(Eq. 2)}$$

Eq. 2 is novel, distinguished by the inclusion of the duty ratio r. c is the total (cross-bridged plus not-cross bridged) concentration of assembled myosin monomers and c_o is the steady-state value. The second term on the right-hand side captures the effects of both regulating r and also fluctuations in the number of myosin monomers assembled into a myosin mini-filament. $T(c,r)$ is antiparallel to the direction of $K(l)$ (Fig. 1c), which is the net elastic force of an actin segment.

Each actin segment is modeled as a pre-stressed, linearly-elastic rod. Force-extension experiments found that the stiffness of a single actin-filament (with and without tropomyosin) was almost constant (linearly elastic) in the range of 35-170 pN tensile force (*22*). The length changes for single filaments of composite actin/tropomyosin were 0.02-0.06% of the unstressed length per pN of tensile force. These experimental observations support modeling each actin segment as linearly elastic, where the actin segments are pre-stressed by the local cytoskeleton.

To determine the pre-stress in an actin segment of a contractile unit, momentarily visualize that segment as being straight (along the dashed line, from cross-link to cross-link, in Fig. 1c) with a total length $x_1 + x_2$. x_1 is the length of the segment fraction from cross-link 1 to the center of the cross-bridge attachment site and x_2 is the length of the segment fraction from the center of the attachment site to cross-link 2 (when the segment is straight). The segment fractions are pre-stressed a distance d_1 and d_2 (extension

corresponds to positive values and compression corresponds to negative values for d_1 and d_2). Thus the equilibrium lengths for the two segment fractions are x_1-d_1 and x_2–d_2, respectively.

Now return to the deflection geometry shown in Fig. 1c and assess the forces acting on the cross-bridge attachment site. This geometry is consistent with experimental observations of myosin cross-bridging leading to relatively localized bending (centered on the attachment site) of the actin filaments (*23*). Recall that the contraction force *T(c,r)* is the component of the actomyosin force along the deflection direction. The net elastic force *K(l)* is the vector sum of $\boldsymbol{f}_{elastic,1}$ and $\boldsymbol{f}_{elastic,2}$, which are the linearly elastic forces of two segment fractions. The magnitudes of $\boldsymbol{f}_{elastic,1}$ and $\boldsymbol{f}_{elastic,2}$ are:

$$f_{elastic,1}(s_1) = k[s_1 - (x_1 - d_1)] \quad \text{(Eq. 3)}$$

$$f_{elastic,2}(s_2) = k[s_2 - (x_2 - d_2)] \quad \text{(Eq. 4)}$$

where k is the Hookean constant. Then $K(l)$ is given by:

$$K(l) = f_{elastic,1}(s_1)\, sin\theta_1 + f_{elastic,2}(s_2)\, sin\theta_2 \quad \text{(Eq. 5)}$$

θ_1 and θ_2 are the angles between the segment fractions and the dashed line. It is straightforward but tedious to simplify Eq. 5. First, solving for s_1:

$$s_1 = x_1\sqrt{1 + (\frac{l}{x_1})^2} \quad \text{(Eq. 6)}$$

Similarly for s_2:

$$s_2 = x_2\sqrt{1 + (\frac{l}{x_2})^2} \quad \text{(Eq. 7)}$$

Second, $sin\theta_1 = \frac{l}{s_1}$ and $sin\theta_2 = \frac{l}{s_2}$. Insert Eqs. 3 and 4 and these two trigonometric definitions into Eq. 5, then substitute Eq. 6 and Eq. 7 for s_1 and s_2. Third, the force-balance condition in the deflection direction is $T(c_o,r) = K(l_o)$. Now use a Taylor Series expansion about the steady-state value l_o for each of the two square-root terms. After some algebra, it can be shown (to third order):

$$K(l) = K(l_o) + k_1(l - l_o) + k_3(l - l_o)^3 \quad \text{(Eq. 8)}$$

where $k_1 = k\left(\frac{d_1}{x_1} + \frac{d_2}{x_2}\right)$ and $k_3 = \frac{k}{2}\left(\frac{x_1 - d_1}{{x_1}^3} + \frac{x_2 - d_2}{{x_2}^3}\right)$. The linear-term k_1 vanishes when $d_1 = d_2 = 0$ (no pre-stress). Thus this intrinsic nonlinear elasticity $k_3 (l - l_o)^3$ is a geometrical effect that arises when linearly elastic actin filaments are deflected.

We have carried out an order-of-magnitude estimate of the segment deflection, recognizing that actin filaments bend more readily than they elongate (*18*). Each of the two actin segments in a contractile unit was idealized as having a length L_{seg}. Each segment is cross-linked to two neighboring actin filaments, where each of the four neighboring actin filaments was idealized as having a length $L_{neighbor}$. To keep the mathematics tractable, the neighboring actin filaments were modeled as cantilevered beams (*18*, page 103). Initially both the neighboring actin filaments and the actin segments were straight. Actomyosin forces then changed the shape of the contractile unit and the four neighboring actin filaments as the forces balanced. More specifically, both actin segments deflected and each of the four neighboring actin filaments bent (moving the four cross-links). We used L_{seg} = 0.5 μm and $L_{neighbor}$ =1 μm as representative values and we used the experimental value for the flexural rigidity of actin-tropomyosin (*18*, Table 8.1). Factoring in both geometry and the steric constraint, we estimated $T(c_o,r)$ as *0.1 pN*. The orders of magnitude for both l_o and the change in cross-link spacing were 100 nm. These estimates are biologically significant, consistent with numerous contractile units driving relevant distortions of the apicomedial cytoskeleton.

Turnover of myosin mini-filaments

We model the steady-state myosin mini-filament as an assembly of 16 myosin-2 monomers. In addition, we assume an assembled mini-filament exhibits turnover, i.e., the number of assembled monomers $N(t)$ can deviate about this steady-state (reference) value N_o=16. There are supportive experimental observations about myosin assembly and disassembly, albeit indirect. For *Acanthamoeba*, three sequential lateral dimerization steps (antiparallel monomers, dimers, tetramers, and then octamers) produce a 232-nm long myosin-2 mini-filament characterized by a bare zone and two ends, each decorated with eight myosin heads (*24*). In contrast, for vertebrate skeletal muscle the assembly mechanism involves nucleation (lateral anti-parallel dimer assembly to produce the bare zone) followed by an elongation process (parallel dimer assembly at each end) to produce a 1.57 μm (myosin) thick filament (*25*). Following nucleation, the mechanism for assembly and disassembly is via parallel dimers coming on and off the ends, respectively. For human non-muscle myosin-2, electron micrographs of three paralogs quantified length distributions of 301±24 nm, 323±24 nm, and 203±33 nm (*26*). The assembly and

disassembly mechanisms for *Drosophila* myosin-2 mini-filaments (360 nm length) are not as thoroughly studied at this time, but it is thought they follow a plan of nucleation and elongation. Electron micrographs of *Drosophila* myosin-2 mini-filaments (*16*) are consistent with three sequential anti-parallel assembly steps (nucleation) followed by two sequential (at each end) parallel dimer steps (elongation), yielding 14.9±3 monomers. One interpretation of this account is myosin mini-filaments are monodispersed in size and the reported uncertainties reflect harsh experimental methods (*16,26*). An alternative interpretation is the elongation process admits size distributions, which is consistent with two recent findings regarding myosin kinetics. First, the partitioning of 300 nm myosin-2 mini-filaments has been investigated in fibroblasts (*27*). The fluorescence intensity of individual mini-filaments doubled just prior to partitioning. Second, myosin-2 turnover has been investigated in REF52 cells where 300±20 nm mini-filaments form stacks (*28*). Turnover had a characteristic half-life of 60 s and was independent of actin dynamics. Given these supportive biological observations, we model deviations in the number of monomers assembled in a myosin mini-filament, however, we cannot rule out dimer (or other) deviations. We also cannot rule out an alternative model for deviations based on an unknown regulatory mechanism that would reduce the activity to zero for a fraction of the myosin heads on each end of a myosin mini-filament. Fig. 1d portrays the kinetic pathways at one end of a myosin mini-filament for assembled myosin and free myosin monomers.

Our turnover equation, which introduces the effect of myosin cross-bridging/regulation in addition to volume changes in chemical kinetics, tracks deviations in the concentration of monomers in an assembled myosin mini-filament. The turnover equation for a myosin mini-filament end is:

$$\frac{dc}{dt} = -\frac{c-c_o}{\tau(1+r)} - \frac{c}{V}\frac{dV}{dt} \qquad \text{(Eq. 9)}$$

where V is the volume local to this end. The first term on the right-hand side includes the duty ratio r [the average lifetime of an assembled monomer is $\tau(1+r) = \frac{1}{k_d}$, where k_d is the dissociation constant].

Eq. 9 is a novel extension of generic turnover equations. More specifically, turnover equations for various dimensions have been applied to the cytoskeleton in the past (e.g., *29,11-13*). The generic 3-D turnover equation is:

$$\frac{dc}{dt} = k_a - k_d c - \frac{c}{V}\frac{dV}{dt} \qquad \text{(Eq. 10)}$$

where k_a is the association constant. The three chemical species for myosin are free (unassembled) monomers, monomers assembled in myosin mini-filaments but not cross-bridged to an actin segment, and assembled monomers that are cross-bridged to an actin segment. c is the total (cross-bridged plus not-cross bridged) concentration of assembled myosin monomers. The right-most term in Eq. 10 vanishes when the volume is constant, producing a more familiar kinetic equation.

The duty ratio affects the average lifetime of an assembled monomer. To see this, consider the special case where $c=c_o$ and $\frac{dc}{dt} = \frac{dV}{dt} = 0$. In this steady state Eq. 10 simplifies to $k_a = k_d c_o$, where $k_d = \frac{1}{\tau(1+r)}$. $\tau(1+r)$ is the average lifetime of an assembled monomer, which takes into account the concentration c referring to both the cross-bridged plus the not cross-bridged myosin monomers, whereas the dissociation process is from not-cross-bridged, assembled monomers to free monomers. In other words, the nominal lifetime τ (for a monomer assembled in a myosin mini-filament) has been increased by a multiplicative factor of $(1+r)$ due to assembled and cross-bridged myosin monomers being chemically distinct from assembled monomers that are not cross-bridged to actin segments. The duty ratio can be expressed in multiple forms:

$r = \frac{\frac{1}{k_{on}}}{\frac{1}{k_{on}}+\frac{1}{k_{off}}}$ or, equivalently, $r = \frac{t_{on}}{t_{on}+t_{off}} = \frac{t_{on}}{T_{cycle}}$, where t_{on} is the average time a myosin head is attached to actin, t_{off} is the average time it is detached, and their sum $t_{on} + t_{off}$ is T_{cycle}, the period of a cycle (*18*). Substituting for k_a and k_d, Eq. 10 becomes Eq. 9. The next subsection will identify $r(t)$ as the control parameter regulating contractile dynamics.

Expressing Eq. 9 in terms of concentrations is a natural choice for assessing chemical kinetics. In preparation for assessing force production by contractile units, however, we re-express Eq. 9 in terms of the number $N(t)$ of assembled monomers, where

$N(t)=c(t)V(t)$ is the number of monomers in a myosin mini-filament. Making this substitution eliminates the second term on the right-hand side of Eq. 9, yielding:

$$\frac{dN}{dt} = -V\frac{\frac{N}{V}-\frac{N_o}{V_o}}{\tau(1+r)} = -N_o\frac{\frac{N}{N_o}-\frac{V}{V_o}}{\tau(1+r)} \quad \text{(Eq. 11)}$$

The length $l(t)$ and number $N(t)$ can be expressed in terms of their deviations δl and δN from their steady-state values l_o and N_o, respectively:

$$l(t) = l_o(1+\delta l) \quad \text{(Eq. 12)}$$

$$N(t) = N_o(1+\delta N) \quad \text{(Eq. 13)}$$

The role of the local volume in Eq. 9 is to track the concentration of assembled myosin monomers and, equivalently, the role in Eq. 11 is to track the number density of assembled monomers. The local volume $V(t)$ is modeled as a cylinder with its z-axis passing through a mini-filament end and its base separating the mini-filament into two halves. Since a myosin mini-filament has two ends, each contractile unit has two local volumes. The volume of such a cylinder is:

$$V = \pi\left[r_{cyl}(1-\delta l)\right]^2 L_o(1-\delta l) \quad \text{(Eq. 14)}$$

Generally the value of the radius r_{cyl} is halfway to the nearest myosin mini-filament in the lateral directions and the height L_o of the cylinder is halfway to the nearest myosin mini-filament in the longitudinal direction. Recall $\delta l>0$ is an inward deflection, so changes in the radius and height are tracked through the two $(1-\delta l)$ terms in Eq. 14. Recognizing that $V_o = \pi\, {r_{cyl}}^2 L_o$, the ratio $\frac{V}{V_o}$ is given by:

$$\frac{V}{V_o} = (1-\delta l)^3 \approx 1-3\delta l \quad \text{(Eq. 15)}$$

We then make three substitutions into the right-most equality in Eq. 11: substitute for $\frac{V}{V_o}$ using Eq. 15 and, based on Eq. 13, substitute both $\frac{dN}{dt}=N_o\frac{d\delta N}{dt}$ and $\frac{N}{N_o} = 1+\delta N$. The resulting expression is:

$$\frac{d\delta N}{dt} = -\frac{3\delta l+\delta N}{\tau(1+r)} \quad \text{(Eq. 16)}$$

Eq. 16 is the turnover equation in terms of the deviations δl and δN from their steady-state values l_o and N_o, respectively.

Contractile unit: steady or oscillating dynamics

This section reports the results of a stability analysis (detailed in Appendix A), which quantifies the parameters for which a contractile unit produces either steady or oscillating forces that distort their local actin network. Steady actomyosin forces would increasingly deflect each actin segment until force balance with the net elastic force is achieved (Fig. 1c). Oscillating actomyosin would cause the segment deflection l(t) to oscillate about the steady value l_o and the number $N(t)$ of monomers assembled into a myosin mini-filament to oscillate about the steady value N_o.

The stability analysis (*30*) characterizes the solutions of the turnover equation (Eq. 16) coupled with the dynamical equation (insert Eqs. 2 and 8 into Eq. 1). The region above the bifurcation line in the phase portrait (Fig. 2a) corresponds to stable oscillations (*29*), recapitulating the oscillations of the Dierke's model (13). Fig. 2 characterizes six oscillating solutions. Increasing the offset above the bifurcation line (solutions shown as red, green, and blue circles in Fig. 2a) corresponds to oscillations of increasing amplitude that are increasingly anharmonic (Fig. 2b-e).

Next we systematically characterized the consequences of moving a solution across the bifurcation line (Fig. 3a) by decreasing the control parameter $r\bar{t_1}$ as time progresses (Fig. 3b). Moving a solution across the bifurcation line, as summarized in Fig. 3, involves a Hopf bifurcation. More specifically, consider a solution that originates below the bifurcation line in a phase portrait, which would be a stable fixed point. Now increase the value of $r\bar{t_1}$ until the solution crosses the bifurcation line and settles into a stable limit cycle. This process is a Hopf bifurcation (*29*). Switching from an oscillation to a steady solution is reversing though a Hopf bifurcation.

Figure 3 demonstrates that the dynamical details are strongly dependent on the final location when reversing through a Hopf bifurcation. The general trend in Panel d is the deeper the offset below the bifurcation line, the more rapid the transition. The red solution corresponds to the deepest offset, where the transition to the fixed point is a relaxation process without overshoot or damped oscillations. The next largest offset is the blue solution, which exhibits one overshoot in Panel d. The next largest offset is the purple solution, which exhibits damped oscillations before settling into the fixed point at ~30 time units. The green solution in panel d, barely below the bifurcation line in Panel a,

exhibits critical slowing (*29*) and has not yet settled into the fixed point at 50 time units. Panel c exhibits a similar pattern in that the deeper the offset from the bifurcation line, the more direct the clockwise inward spiral to the fixed point. In other words, the number of wraps of the clockwise inward spiral decreases with increasing depth below the bifurcation line (Panel d). The solutions for each case were simulated for 50 time units for presentation purposes, which has a strong effect on the green solution. More specifically, this critically slowed clockwise inward spiral has been truncated to leave an open core so as not to obscure the other three cases. Increasing the simulation beyond 50 time units would progressively fill the open core with space filing green spirals.

In summary, when reversing through a Hopf bifurcation the solution that initially was a stable oscillation switches to a steady force (in contrast to a quiescent state) and deepening the offset below the bifurcation line (Fig. 3a) decreases the number of wraps and shortens the transition time (Fig. 3c,d).

Boosting the piconewton contractile-unit forces to nanonewton cytoskeletal forces

The preceding subsections have been focused on the dynamics of molecular contractile units (Fig. 1a,b). Now we turn our attention to the collective effect of numerous contractile units distributed throughout the apicomedial cytoskeleton of an amnioserosa cell (Fig. 1 e,f). We invoke elastic percolation theory (Appendix B), where there is compelling experimental evidence that reconstituted model cytoskeletons are consistent with elastic percolation theory (*31,32*). The generic term "cluster" from this theory, in our application, refers to more than two actin filaments connected by cross-links, where the hallmark of elastic percolation theory is such cross-links are randomly distributed among all possible paired binding sites in the actin network.

Adherens junctions and disordered contractile units can each exert stresses on a cross-linked actin network. Stress transmission throughout the actin network depends on cross-links that can bear stress. The dotted oval in Fig. 1e encircles one cluster that includes three contractile units. This cluster, however, is not connected via cross-links to the junctional belt and would not change the cell shape. In contrast, each of the other three clusters in Fig. 1e are multiply connected to the junctional belt and contractile-unit forces produced within each of these clusters could change the cell shape. A remarkable feature of elastic percolation theory (Appendix B) is that the cytoskeletal forces will scale

relative to contractile-unit forces, where the scaling factor is $[p(f) - p_c]^4$ (*33,34*). Here *p(f)* is the probability of a crosslink at any potential cross-linking site and p_c is the critical threshold for the first cluster making contact with junctional belts at two locations. Further increase in $p(f)$ above p_c is accompanied by an increasing preponderance of parallel networks of contractile units in the cross-linked apicomedial cytoskeleton.

Cross-links undergo binding and unbinding events that can exhibit catch and/or slip bond dynamics. Here we treat the cross links as slip bonds, consistent with the model of Bell (*34*) and the experimental observations of Alvarado, et al (*31*). Bell has modeled the stress-dependence of unbinding slip bonds (*34*), where the unbinding rate $k_{off}(f)$ is summarized by Bell's Equation:

$$k_{off}(f) = k_{off,o}\, e^{\frac{f}{f_o}} \qquad \text{(Eq. 17)}$$

where *f* is the net force exerted on a cross-link by the two actin filaments. $k_{off,o}$ is the unbinding rate when f=0. f_o is deduced from the potential energy surface for the cross-link bond. Thus the unbinding constant increases exponentially as it bears stress.

Alvarado, et al., extended Bell's Equation to include the possibility that a cross-linking molecule could rebind shortly after unbinding (*31*). Upon unbinding, v is the relative speed of the two liberated actin filaments. If v is sufficiently slow, the cross-linking molecule can remain within the proximity of the original actin binding site such that the probability for rebinding to the original site $e^{-\frac{v_o}{v}}$ is significant. The reference speed v_o corresponds to $k_{on}c_x d$, where k_{on} is the binding rate, c_x is the concentration of cross-linking molecules, and d is a measure of the size of the binding site. Consequently the effective stress-dependent unbinding rate $k_{off}(f)$ is given by:

$$k_{off}(f) = k_{off,o}\, e^{\frac{f}{f_o}}\, e^{-\frac{v_o}{v}} \qquad \text{(Eq. 18)}$$

Given k_{on} and $k_{off}(f)$, the probability $p(f)$ for a cross-link can be modeled with the Hill equation (n=1).

$$p(f) = \frac{1}{1+\frac{K_d(f)}{c_x}} \qquad \text{(Eq. 19)}$$

where

$$K_d(f) = \frac{k_{off}(f)}{k_{on}} = \frac{k_{off,o}}{k_{on}} e^{\frac{f}{f_o}-\frac{v_o}{v}} \qquad \text{(Eq. 20)}$$

Experiments have demonstrated that global cytoskeletal contractions require a reduction in myosin motor activity, which seems counterintuitive but has been quantitatively accounted for in terms of the stress dependence of actin cross-linkers and the role they play in cytoskeletal stress propagation (*31*). This experimental observation is consistent with our mechanochemical mechanism in that ceasing oscillations necessitated moving the solution across the bifurcation line by decreasing the control parameter $r(t)$ (Fig. 2), which decreases the contractility (Eq. 2). We attribute decreasing $r(t)$ to myosin regulation (*11,36,37*). Reducing $r(t)$ triggers a remarkable mechanochemical and percolation cascade. More specifically, decreasing $r(t)$ proportionally reduces the local stresses exerted on cross-links by contractile units to exponentially reduce $k_{off}(f)$ (Eq. 20). Thus $p(f)$ increases as does the connectivity and consequently increases cluster size and branching complexity (compare Fig. 1e,f), which is consistent with previous results (*31*, and references therein). Scaling is a consequence of progressively extensive parallel branching.

Intercellular forces

Cell-shape changes are a consequence of (applied) force imbalance along common cell junctions between neighboring cells. During oscillations of apical cross-sectional areas, the direction of net intercellular force imbalance varies both along the cell junctions and as a function of time (*7*). During an ingression process, the magnitude of the net force imbalance along the common cell junctions increases substantially and essentially all of these net forces are pointed inwards from the perspective of the ingressing cell.

The increase of the cytoskeletal forces of an ingressing cell relative to its neighboring, non-ingressing cells can be quantified with elastic percolation theory. The average cytoskeletal force from the ingressing cell on a common cell junction is $F_{ing}(r_{ing})$ and for a neighboring cell on that junction is $F_{osc}(r_{osc})$, where $r_{ing} < r_{osc}$. Applying Hooke's Law on that common cell junction, $F_{ing}(r_{ing})=\kappa(r_{ing})\Delta x$ and $F_{osc}(r_{osc}) = \kappa(r_{ing})\Delta x$. Δx is the motion of the common cell junction. The magnification factor M is defined by $F_{ing}(r_{ing}) = M\, F_{osc}(r_{osc})$. Inserting $\kappa(r)= \kappa[p(r)- p_c]^4$ into both average forces, the magnification factor M is given by:

$$M = \frac{F_{ing}(r_{ing})}{F_{osc}(r_{osc})} = \left[\frac{p_{ing}(r_{ing})-p_c}{p_{osc}(r_{osc})-p_c}\right]^4 \quad \text{(Eq. 21)}$$

Numerical simulations indicate the average force exerted on a cell junction by an ingressing cell can exceed that of a neighboring, non-ingressing cell by a factor of 1000 or more (Fig. 3f). Furthermore, the cross-link density indicates the cytoskeleton is relatively compliant (soft) in an oscillating cell and stiffens substantially in an ingressing cell.

Recapitulating experimental data

This section describes a validation-step for this mechanochemical model, which compared *in vivo* confocal measurements of the apical cross-sectional area of three amnioserosa cells during dorsal closure in *Drosophila* (*7*, Fig. 1e) to numerical simulations of time series of these apical areas. These experimental time series exhibited oscillations about a background, which for about half of the cells was shoulder shaped. The oscillations and the shoulder-shaped background were analyzed in parallel. Fourier analyses of experimental observations indicate the apical-area oscillations essentially are harmonic and exhibit a band of frequencies centered at 5.7±0.9 mHz, where each oscillator initially was reversible and then progressively decreased in area amplitude.

The shoulder-shaped background was quantified with an ingression function $I_i(t)$ (*7*):

$$I_i(t) = \frac{\alpha_i}{2}[1 - \tanh(\varepsilon_i\, t - \tau_i)] \quad \text{(Eq. 22)}$$

The index *i* identified the amnioserosa cells, which each had an initial area α_i. The imaging time is *t*, with *t=0* corresponding to the first confocal image. $\frac{\tau_i}{\varepsilon_i}$ is the time of the inflection point, when the slope is $\frac{\alpha_i \varepsilon_i}{2}$.

The time dependence for down-regulating the duty ratio $r_i(t)$ tracked the time dependence of Eq. 22:

$$r_i(t) = r_{final,i} + (\frac{r_{initial} - r_{final,i}}{2})[1 - \tanh(\varepsilon_i\, t - \tau_i)] \quad \text{(Eq. 23)}$$

The values for ε_i and τ_i were determined by fitting of the experimental background shoulder with Eq. 22 (*7*). The experimental value for the duty ratio $r_{initial}$ is 0.10 (*19*). Note that the duty ratio $r_i(t)$ is the control parameter that moves the solution $(r\bar{t}_1,\ \frac{1}{\bar{\tau}\,(1+r)})$ on the phase portrait.

Our systematic investigation of the effect of the location of the solutions on the phase portrait informed our choices for $r_{initial}$ $\bar{t}_1$ and r_{final}. First, the experimentally observed harmonic oscillators indicate the initial parameters are just above the bifurcation line (Fig. 2) and that location was chosen to match the experimental amplitude of oscillation. Second, the depth of the final parameters determines the decay of the oscillations once ingression commences, i.e., the number of wraps as the oscillator decayed to the fixed point (Fig. 3). The depth was chosen to match the rate of oscillator decay in each of the three experimental time series.

Recapitulating the data required summing at least five classes of oscillators with distinct parameter sets (Fig. 3e), where each class of oscillator corresponds to numerous entrained contractile units (*38*). We systematically explored how many distinct classes needed to be summed to semi-quantitatively recapitulate the data. More specifically, one class was too regular. More than one class with different frequencies $\bar{\omega}_i = \frac{1}{\sqrt{\bar{\tau}_i(1+r)}}$ (Appendix A) introduced the desired interference, where the simulated time series depends on the values for $\bar{\tau}_i$, the relative amplitudes of the oscillators, and any phase shifts. Incrementing the number of oscillator classes, we found that five classes started to reasonably recapitulate the data and that six classes did not lead to noticeable improvement.

The numerical simulations summed $I_i(t)$ and a set of five area oscillators, which were synchronized by their inflection points, to produce Fig. 3e. The parameters of the five oscillators for each of the three time-series of the cross-sectional areas of amnioserosa cells presented in Fig. 3e are listed in Table 1. The frequencies were selected by systematically varying $\bar{\tau}$ and were roughly centered about $\bar{\tau}$=1, which were then rendered dimension-full so that scaled values were within the experimental bandwidth and centered on its central frequency. In each case, the sum of the five oscillator classes was scaled to reproduce the relative amplitudes from the experimental data (*7*). Each of the simulated time series compares favorably with the corresponding experimental time series (*7*, Fig. 1e) and was based on a monomer deviation of about $^{+6}_{-7}$ % for the blue trace (less for green and red traces). This compares favorably with the experimental uncertainty of 14.9±3 (20%) (*16*). The red trace corresponds to a fast switching cell that

ingresses quickly. The green and blue traces are cells that switch and ingress more slowly.

Table 1

Parameters used in generating Fig. 3e

Oscillator Number	$r_{initial}\ \bar{t_1}$	$\frac{1}{\bar{\tau}}$	Relative Amplitude	r_{final}	ε	Phase
Red Trace				0.030	0.330	
1	2.1	0.6	0.5			4
2	2.3	0.8	0.5			0
3	2.5	1.0	1.0			0
4	2.6	1.1	0.5			0
5	2.7	1.2	0.5			3
Green Trace				0.065	0.053	
1	2.1	0.6	0.5			0
2	2.3	0.8	0.5			0
3	2.5	1.0	1.0			0
4	2.6	1.1	0.5			0
5	2.7	1.2	0.5			0
Blue Trace				0.065	0.038	
1	2.1	0.6	0.5			0
2	2.3	0.8	0.5			0
3	2.5	1.0	1.0			0
4	2.6	1.1	0.5			0
5	2.7	1.2	0.5			0

Fig. 3e is a proof-of-principle that five classes of numerical area oscillators based on this mechanochemical mechanism can semi-quantitatively recapitulate each of these three experimental time series, where each parameter set is not unique. We attribute the distribution in oscillator frequencies to variable geometries of the contractile units (Fig. 1c). More specifically, the time scale is $\frac{\mu}{k_1}$ and, as derived earlier, $k_1 = k\left(\frac{d_1}{x_1} + \frac{d_2}{x_2}\right)$.

Discussion

These results indicate that oscillations in apical areas, the switching process, and cell ingression are manifestations of one multi-scale, mechanochemical mechanism operating in different parameter regimes. Once assembled a contractile unit could settle spontaneously into oscillations without requiring fine-tuning of either the monomer number or the initial deflection. Down regulating as opposed to upregulating the actomyosin force ensures that the contractile units have the dynamic range to quickly trigger ingression without the need to assemble additional contractile units. Incidentally decrementing the value of the duty ratio, but remaining above the bifurcation line as an oscillating solution, mimics a ratchet mechanism. These observations indicate that: cell oscillations can be a dynamical holding pattern; regulating *r(t)* to alter cross-link dynamics is a nimble switch; and ingression can be a key driver of tissue dynamics and morphogenesis (*8,39,40*).

These results are relevant to several unresolved research questions in tissue biomechanics. Conjectures regarding a "clutch" that engages the apicomedial cytoskeleton to cell junctions (*41*) and "how increased myosin activity gives rise to cells that contract very slowly" (*42*) are consistent with establishing and rupturing percolating pathways of cross-linked actin clusters, respectively. Reports of actin and/or myosin exhibiting reversible and stage-dependent apicomedial coalescence, persistence, pulsation, and intense foci in addition to increased myosin activity leading to both abnormally compacted networks and the suppression of ingression (*36,37*) are consistent with the dynamics of percolating and non-percolating (disconnected islands) cluster dynamics. Hu, et al., have proposed a mechanism, mediated by the disordered actin network, for long-range interactions between myosin mini-filaments in REF52 cells (*28*). This proposal is suggestive of cluster dynamics. The results presented here promise

quantitative tests of how the mechanochemical and percolation cascade augments myosin's regulatory network (*36,37,43,44*, reviewed in *11*). For example, increasing myosin activity would increase the duty ratio, the filament duty ratio, and the contractile-unit forces with the downstream effects of disrupting actin cross-links, reducing the number and parallelness of percolating pathways, and reducing the magnification of cytoskeletal forces. We have found that regulating myosin can change the "gear" of contractile units, switching from oscillations to steady-forces, and that counter-intuitive downstream effects (*31*) can boost piconewton molecular forces into nanonewton cytoskeletal forces. These observations highlight the importance of the biological and biomechanical mechanisms for regulating myosin activity during development.

Appendix A: Stability analysis

We performed a stability analysis (*30*) of the 3D turnover equation (Eq. 16), which affects how many myosin monomers are assembled and contributing cross-bridges to generate the actomyosin force, coupled with the dynamical equation in the deflection direction that was presented as Eq. 1, reproduced here for convenience:

$$\mu \frac{dl}{dt} = T(c,r) - K(l)$$

We now re-express Eq. 1 in terms of δl and δN, paralleling the process we used to convert Eq. 11 into Eq. 16.

Eq. 2 linearized the contraction force about its steady-state value, i.e., $T(c,r)=T(c_o,r)+ rt_1(c-c_o)$. Inserting Eq. 2 for $T(c,r)$ and Eq. 8 for $K(l)$, Eq. 1 becomes:

$$\mu \frac{dl}{dt} = [T(c_o,r) + rt_1(c-c_o)] - [K(l_o) + k_1(l-l_o) + k_3(l-l_o)^3] \quad \text{(Eq. A1)}$$

Since $T(c_o,r) = K(l_o)$ (steady-state force balance), these terms cancel in Eq. A1, resulting in:

$$\mu \frac{dl}{dt} = rt_1(c-c_o) - k_1(l-l_o) - k_3(l-l_o)^3 \quad \text{(Eq. A2)}$$

We then make the following substitutions to re-express Eq. A2 in terms of the deviation δl about its steady-state value l_o. Based on Eq. 12, we substitute both $\frac{dl}{dt} = l_o \frac{d\delta l}{dt}$ and $l-l_o = l_o\, \delta l$, yielding:

$$\mu l_o \frac{d\delta l}{dt} = rt_1(c-c_o) - k_1 l_o \delta l - k_3(l_o \delta l)^3 \quad \text{(Eq. A3)}$$

The first term on the right-hand side, $rt_1(c\text{-}c_o)$, can be rewritten as $rt_1c_o(\frac{c}{c_o} - 1)$. $\frac{c}{c_o}$ is equal to $\frac{\frac{N}{V}}{\frac{N_o}{V_o}} = \frac{\frac{N}{N_o}}{\frac{V}{V_o}}$. Using Eq. 15 to substitute $1 - 3\delta l$ for $\frac{V}{V_o}$ and Eq. 13 to substitute $1+\delta N$ for $\frac{N}{N_o}$, Eq. A3 becomes:

$$\mu l_o \frac{d\delta l}{dt} = rt_1c_o\left(\frac{1+\delta N}{1-3\delta l} - 1\right) - k_1 l_o \delta l - k_3(l_o\delta l)^3 \qquad \text{(Eq. A4)}$$

We now convert Eqs. 16 and A4 into dimensionless forms, where the dimensionless parameters are $\bar{t} = \frac{k_1}{\mu}t$, $\bar{\tau} = \frac{k_1}{\mu}\tau$, $\overline{t_1} = \frac{3c_o}{k_1 l_o}t_1$, and $\overline{k_3} = \frac{{l_o}^2}{9k_1}k_3$. We also substitute $\overline{\delta l} = -3\delta l$, which includes a minus sign such that a positive value for $\overline{\delta l}$ corresponds to an expansion of the contractile unit. With these substitutions, the dimensionless forms of the dynamical (Eq. A4) and turnover (Eq. 16) equations are:

$$\frac{d\overline{\delta l}}{d\bar{t}} = -r\overline{t_1}\left(\frac{1+\delta N}{1+\overline{\delta l}} - 1\right) - \overline{\delta l} - \overline{k_3}\,\overline{\delta l}^{\,3} \qquad \text{(Eq. A5)}$$

$$\frac{d\delta N}{d\bar{t}} = \frac{\overline{\delta l} - \delta N}{\bar{\tau}\,(1+r)} \qquad \text{(Eq. A6)}$$

The determination of the bifurcation line is based on linearized forms of the coupled nonlinear equations (*30*). Linearizing Eq. A5 requires a series expansion of the denominator $1+\overline{\delta l}$, which excludes the solution $\overline{\delta l} = -1$. After some tedious algebra, the linearized form of Eq. A5 is:

$$\frac{d\overline{\delta l}}{d\bar{t}} = (r\overline{t_1} - 1)\overline{\delta l} - r\overline{t_1}\delta N \qquad \text{(Eq. A7)}$$

The eigenvalues are $\lambda_{\pm} = R \pm i\overline{\omega}$, where:

$$R = \frac{(r\overline{t_1} - 1)\bar{\tau}\,(1+r) - 1}{2\,\bar{\tau}\,(1+r)} \qquad \text{(Eq. A8)}$$

$$\overline{\omega} = \frac{\sqrt{4\bar{\tau}\,(1+r) - [1+\bar{\tau}\,(1+r) - r\,\overline{t_1}\,\bar{\tau}\,(1+r)]}}{2\,\bar{\tau}\,(1+r)} \qquad \text{(Eq. A9)}$$

The bifurcation occurs when R=0. Setting R to 0 in Eq. A8 yields:

$$r\overline{t_1} = 1 + \frac{1}{\bar{\tau}\,(1+r)} \qquad \text{(Eq. A10)}$$

This has a particularly nice form, where both the intercept and the slope are 1 (Figs. 2a, 3a). Inserting Eq. A10 into Eq. A9, we find that the dimensionless frequency of the limit cycle as R becomes non-negative is $\overline{\omega_o} = \frac{1}{\sqrt{\bar{\tau}\,(1+r)}}$, which increases in value as

$\bar{\omega} = \bar{\omega_o}\sqrt{1+\frac{R}{2}}$ as the solution begins to move above the bifurcation line.

These results should be considered along with the discussion of the steady state in the subsection on the nonlinear elasticity of the contractile unit. A steady solution corresponds to $l(t)=l_o$, portrayed in Fig. 1c. An oscillating solution corresponds to $l(t)=l_o[1+\delta l(t)]$, which is an oscillation about l_o with a frequency $\bar{\omega}$ (Figs. 2d,e). Furthermore, oscillations in the segment deflections are accompanied by oscillations in the positions of the four cross-links and oscillations in the distortion of the local cytoskeleton.

Tutorial on interpreting phase portraits

This section provides an account for how the solutions to these coupled, nonlinear equations can be characterized with multiple plots. Phase portraits, which are plots of the dimensionless contractility parameter $r\bar{t_1}$ versus the dimensionless turnover parameters $\frac{1}{\bar{\tau}\,(1+r)}$ in Figs. 2a and 3a, or $\bar{t_1}$ versus $\frac{1}{\bar{\tau}}$ in Fig A1a, visualize the two classes of solutions. More specifically, a bifurcation line separates an upper region of stable limit cycles (oscillations) from a lower region of stable fixed points (steady forces). Time series (Fig. 2d,e, 3d, A1d,f) visualize (the approach to) steady or oscillating solutions. Plots of normalized number versus normalized deflection (Figs. 2b,c, 3c, A1c) visualize the limit cycles, i.e., the tradeoff between number (correlates with stress) and deflection (strain).

Figure A1 can serve as a tutorial in synthesizing information from these multiple plots. Consider the blue circle in Fig. A1a, which is a solution in the stable fixed-point region. This solution corresponds to the blue curves in the other panels of Fig A1. In Panel d the steady-state solution is $\frac{l}{l_o}$ =1. The deflection l initially was arbitrarily chosen to be less than l_o, but subsequently approaches the fixed-point value l_o. In Panel f the initial number of assembled monomers N was arbitrarily chosen to be less than N_o. Similar to l, N subsequently approaches the fixed-point value N_o. In Panel c the fixed point is located at $\frac{N}{N_o} = \frac{l}{l_o} = 1$. The initial values for $\frac{N}{N_o}$ and $\frac{l}{l_o}$ are indicated by the blue circle and the subsequent approach to the fixed point is the blue curve connecting that

circle to the fixed point at $\frac{N}{N_o} = \frac{l}{l_o} = 1$. Thus the subsequent approach from the initial location is a transient counterclockwise spiral towards the stable fixed-point.

Next consider the red circle in Fig. A1a, which is a solution in the stable limit-cycle region. Paralleling the discussion of the previous paragraph, this solution corresponds to the red curves in the other panels of Fig A1. In Panel d the initial choice for the red curve is very close to the reference value l_o. l eventually settles into stable oscillations. In Panel c the red curve originates near the reference values $\frac{N}{N_o} = \frac{l}{l_o} = 1$ and exhibits a transient counterclockwise, outward spiral to the stable limit cycle (the outermost red orbit). For both the blue and red results in Panel c, for any initial location the system will be attracted to its stable solution, transiently spiraling into its fixed point or limit cycle and becoming stable, respectively.

Comparison with Dierkes, et al.

This section compares and contrasts our mechanochemical model with that of Dierkes, et al. (*13*). The Dierkes model demonstrates spontaneous nonlinear oscillations; however, the cross-sectional area of an amnioserosa cell was treated as a single 1-D contractile unit (equivalent mechanical circuit). Motivated by their mathematical insight, we have formulated a 3-D model for spontaneous oscillations based on the dynamics of a molecular contractile unit and have characterized an intrinsic nonlinear elasticity. Furthermore, we have extended the nonlinear dynamics to account for ingression. We also have addressed the conundrum of how to boost piconewton actomyosin forces to nanonewton cytoskeletal forces to drive cell-shape changes with an application of percolation theory.

There is a notational issue that addresses the qualitative difference between Fig. 3c and Fig. A1c. $\overline{\delta l}$ in our notation corresponds to δl in the notation of Dierkes, et al. Or equivalently, $-3\delta l$ in our notation corresponds to δl in the notation of Dierkes, et al. This accounts for the clockwise approach in Fig. 3c and the counter-clockwise approach in Fig. A1c.

While the Dierkes' model differs from our model in biological and physical approaches, it is possible to draw a mathematical equivalence. The set of parameters invoked to arrive at the dimensionless forms in the two models are not identical, but the

equivalence can be drawn when comparing dimensionless equations. Our stability analysis culminated in the dimensionless Eqs. A5 and A6, which explicitly included the effect of the duty ratio *r*. The duty ratio was not considered in the Dierkes' model and needs to be backed out of Eqs. A5 and A6 when pursuing mathematical equivalence. If the duty ratio *r* is set to 0 in Eq. A6, then the resulting equation for δN is mathematically equivalent to Eq. 13 in Dierkes' Supporting Material. If the duty ratio *r* is set to 1 in Eq. A5, then starting with the resulting equation for $\overline{\delta l}$ and substituting a series expansion for $\frac{1+\delta N}{1+\delta l}$ leads to a mathematically equivalent version of Eq. 12 in Dierkes' Supporting Material. Similarly, backing out the duty ratio from the equation for the bifurcation line (Eq. A10) recovers Dierke's version $\overline{t_1}= 1 + \frac{1}{\bar{\tau}}$.

We have reproduced the numerical simulations reported in Dierkes et. al., using their model equations and notation (Fig. A1). Panels a, b, d, and e in our Fig. A1 correspond to Panels b, c, and d in Fig. 2 of Dierkes, et al. We agree with the characterizations that the blue solution is a stable fixed point and the red solution is a stable limit cycle. However, Dierkes, et al, interpreted the green solution as corresponding to the collapse of the cell and speculated that such a collapse could be related to ingression. Following Dierkes' notation, "collapsing" corresponds to $l(t)$ going to zero, i.e., δl reaches a value of minus one in the equation $l(t) = l_o\,(1 + \delta l)$. Inspection of Eq. A5 indicates that δl=-1 is to be excluded as a solution when a series expansion is substituted for the denominator. Thus the simulations are no longer reliable when the amplitude of the spontaneous oscillations reaches -1, which erroneously implies a vanishing apical area. Fig. 2 demonstrates that the limit cycles grow larger and the amplitudes of the oscillations get larger with increasing offset above the bifurcation line in the phase portrait. The dashed line in the Fig. A1a indicates the threshold for this numerical artifact, where the green solution is above this threshold.

Here we have characterized the decrease in the amplitude of the oscillations to be the consequence of approaching the bifurcation line from above and that ingression (delamination) is the consequence of both a reverse Hopf bifurcation (Fig. 3a-e) and the remodeling of the cross-linked cytoskeleton to magnify the contractile-unit forces (Fig. 1e,f).

Appendix B: Tutorial on percolation theory applied to the cytoskeleton

This section justifies the applicability of elastic percolation theory to account for the nonlinear dynamics of the cytoskeleton. The cytoskeleton is an out-of-equilibrium structural network internally driven by actomyosin complexes (*1*), i.e., by a disordered network of contractile units. It is active in the sense that actomyosin complexes convert chemical energy into mechanical work to internally drive the cross-linked actin network, which bears mechanical stress. Percolation has been applied successfully both to elastic networks in general (*33,34*) and to active, internally-driven model cytoskeletal systems (*31,32*).

The term percolation appeals to the multitude of complex, tortuous paths taken by water as it moves through porous material. Consider each location within the porous material as either being an air pocket with a probability p or being an impenetrable solid with a probability $1-p$. A probability $p=0$ corresponds to a solid rock. Now let p increase above zero. In the following, 1) a cross-link is analogous to the smallest possible air-pocket; 2) a cluster is analogous to a larger, likely irregularly shaped air pocket; and 3) the percolation threshold is when the probability p has been increased such that, in general, a multi-branched, irregularly shaped air pocket first allows for water to flow through the porous material. Remarkably the transition as p increases through the percolation threshold p_c has been shown to obey nonlinear scaling laws (*33*), as quantified below.

The quantitative formalism for random percolation (*33*) begins with the concept of clusters as portrayed in Fig. 1e,f. Here a cluster is more than two actin filaments connected by cross-links. Treat the location of cross-links as being randomly distributed among all possible paired binding sites in the actin network. There are no clusters when the probability of a cross-link $p(f)$ is zero, where f is the same force as in Eq. 18. Cross-links increasingly occur as $p(f)$ increases above zero and would be randomly located throughout the paired binding sites in the actin network. For relatively small values of $p(f)$, there likely would be little if any clusters and, if there were a cluster, it most likely would be relatively small. But as $p(f)$ continues to increase in all likelihood the number and the size of the clusters also will increase. With further increase, $p(f)$ eventually will

cross a critical threshold p_c when one cluster first becomes cross-linked to adherens junctions at two distinct locations, i.e., a percolation pathway is first established. For $p(f) < p_c$, there are no percolation pathways and cell-shape changes would not be driven by this percolating network model of a cytoskeleton. For $p(f) > p_c$, the percolation pathways can drive cell-shape changes. More specifically, the distribution of clusters changes and percolation pathways change as $p(f)$ continues to increase beyond p_c. For relatively small values of $p(f)-p_c$, in all likelihood the clusters are relatively small or stringy, exhibiting relatively few percolation pathways connecting the adherens junctions (Fig. 1e). As $p(f)-p_c$ increases, in all likelihood there will be fewer, larger clusters with complex parallel branches making a relatively large number of connections to the adherens junctions (Fig. 1f). When $p(f)$=1, the probability of cross-linking has reached 100% and all possible cross-links occur.

For an elastic percolating network, extensive research has shown that the network elastic constant $\kappa(r) = \kappa[p(r)- p_c]^4$ (*33,34*), where κ corresponds to the elastic stiffness of a contractile unit and the consensus view is the value of the critical exponent is close to, if not equal to, 4 (*33*).

References

1. F.C. MacKintosh, C.F. Schmidt, Current Opinion in Cell Biology 22, 29 (2010).
2. P.J. Keller, L.A. Davidson, D.R. Shook, Differentiation 71, 171 (2003).
3. P. Hayes, J. Solon, Mech Dev 144, 2 (2017).
4. D.P. Kiehart, J.M. Crawford, A. Aristotelous, S. Venakides, G.S. Edwards, Annual Reviews Cell and Developmental Biology (in press).
5. B.G. Fernandez, A. M. Arias, A. Jacinto, Mechanisms of Development 124, 884 (2007).
6. J. Solon, A. Kaya-Copur, J. Colombelli, D. Brunner, Cell 137, 1221 (2009).
7. A. Sokolow, Y. Toyama, D.P. Kiehart, G.S. Edwards, Biophysical journal 102, 969 (2012).
8. Y. Toyama, X.G. Peralta, A.R. Wells, D.P. Kiehart, G.S. Edwards, Science 321, 1683 (2008).
9. A.C. Martin, M. Kaschube, E.F. Wieschaus, Nature 457, 495 (2009).

10. A.C. Martin, B. Goldstein, Development 141, 1987 (2014).
11. N. Gorfinkiel, Dev Dyn 245, 268 (2016).
12. P.F. Machado, G.B. Blanchard, J. Duque, N. Gorfinkiel, Eur. Phys. J. Special Topics 223, 1391 (2014).
13. K. Dierkes, A. Sumi, J. Solon, G. Salbraux, PRL 113, 148102 (2014).
14. S.-Z. Lin, B. Li, G. Lan, X.-Q. Feng, Proceedings of the National Academy of Sciences USA 114, 8157 (2017).
15. R.R.P. Moore, *Understanding the Organization, Location, and Interactions of Actin-based Structures During Drosophila Dorsal Closure*, Ph.D., Department of Biology, Duke University (2018).
16. D.P. Kiehart, R. Feghali, R, Journal of Cell Biology 103, 1517 (1986).
17. T. Thoresen, R.M. Lenz, M. Gardel, Biophysical journal 100, 2698 (2011).
18. J. Howard, *Mechanics of Motor Proteins and the Cytoskeleton* (Sinauer, Massachusetts, 2001).
19. S.M. Heissler, K. Chinthalapudi, J.R. Sellers, FASEB Journal 29, 1456 (2017).
20. T.L. Hill, *Free Energy Transduction and Biochemical Cycle Kinetics* (Dover Publications, New York, 2005).
21. A.B. Verkhovsky, G.C. Borisy, Journal of Cell Biology 123, 637 (1993).
22. H. Kojima, A. Ishuima, T. Yanagida, T, PNAS 91, 12962 (1994).
23. M.P. Murrel, M.L. Gardel, Proceedings of the National Academy of Sciences USA, 109, 20820 (2012).
24. J.S. Sinard, W.F. Stafford, T.D. Pollard, Journal of Cell Biology 109, 1537 (1989).
25. J.S. Davis, Ann. Rev. Biophys. Biophys. Chem., 17, 217 (1988).
26. N. Billington, A. Wang, A, J. Mao, R.S. Adelstein, J.R. Sellers, Journal of Biological Chemistry 288, 33398 (2013).
27. J.R. Beach, K.S. Bruun, L. Shao, D. Li, Z. Swider, K. Remmert, Y. Zhang, M.A. Conti, R.S. Adelstein, N.M. Rusan, E. Betzig, J.A. Hammer, Nature Cell Biology 19, 85 (2017).
28. S. Hu, K. Dasbiswas, Z. Guo, Y.-H. Tee, V. Thiagarajan, P. Hersen, T.-L. Cheew, S.A. Safran, R. Zaidel-Bar, A.D. Bershadsky, Nature Cell Biology 19, 133 (2017).

29. J. Sedzinski, M. Biro, A. Oswald, J.-V. Tinevez, G. Salbreux, E. Paluch, Nature 476, 462 (2011).
30. S.H. Strogatz, *Nonlinear Dynamics and Chaos: with Applications to Physics, Biology, Chemistry, and Engineering* (Perseus Books Publishing, USA 1994).
31. J. Alvarado, M. Sheinman, A. Sharma, F.C. MacKintosh, G. Koenderink, Nature Physics 9, 591 (2013).
32. M. Sheinman, A. Sharma, J. Alvarado, G.H. Koenderink, F.C. MacKintosh, PRL 114, 098104 (2015).
33. D. Stauffer, A. Aharony, *Introduction to Percolation Theory, 2nd Edition* (Taylor & Francis, London, 1992). Section 5.8.
34. Y. Kantor, I. Webman, PRL 52, 1891 (1984).
35. G.I. Bell, Science 200, 618 (1978).
36. G.B. Blanchard, S. Murugesu, R.J. Adams, A.M. Arias, N. Gorfinkiel, Development 137, 2743 (2010).
37. D.J.V. David, Q. Wang, J.J. Feng, T.J. C. Harris, Development 140, 4719 (2013).
38. A. Zlotnik, R. Nagao, I.Z. Kiss, J-S. Li, Nature Communications 7, 10788 (2016).
39. Y. Yamaguchi, N. Shinotsuka, K. Nonomura, K. Takemoto, K. Kuida, H. Yosida, M. Miura, J. Cell Biol. 195, 1047 (2011).
40. B. Monier, M. Gettings, G. Gay, T. Mangeat, S. Schott, A Guarner, M Suzanne, Nature 518, 245 (2015).
41. M. Roh-Johnson, G. Shemer, C.D. Higgins, J.H. McClellan, A.D. Werts, U.S. Tulu, US, L. Gao, E. Betzig, D.P. Kiehart, B. Goldstein, Science 335, 1232 (2012).
42. S.C. Fischer, G.B. Blanchard, J. Duque, R.J. Adams, A.M. Arias, S.D. Guest, N. Gorfinkiel, PLoS one 9:e95695 (2014).
43. D. Azevedo, M. Antunes, S. Prag, S. Ma, U. Hacker, G.S. Broadland, M.S. Hutson, MS, J. Solon, A. Jacinto, PLoS One 6, e23964 (2011).
44. S. Saravanan, C. Meghana, M. Narasimha, Molecular Biology of the Cell 24, 2350 (2013).

Acknowledgements

Research supported by NIH GM033830. GSE thanks Robert Behringer for insightful comments.

Figure Legends

Figure 1. Modeling cytoskeleton (2D schematics of 3D structures). Myosin mini-filaments are blue, actin filaments are red, and actin cross-links are black dots. Contractile unit (cross-links enumerated, steady-state deflection shaded) shown a) in isolation and b) within a local network. c) Applied forces acting on an actin-segment at the force-balance condition $T(c_o,r) = K(l_o)$, where l_o is the height of the triangle. $f_{ext,1}$ and $f_{ext,2}$ are components (along the segment) of the forces external to the contractile unit. d) Turnover at one end of a myosin mini-filament. e and f) Amnioserosa cell. Light green and dark green borders represent adherens junctions and cell membrane, respectively. The dashed boxes in each lower-left corner correspond to panel b (deflections suppressed). Clusters highlighted in gray. Panel e has four clusters and Panel f has one extensively branched cluster. These Mikado representations of the actin (red) filaments were generated as follows. First, a random distribution of points was generated within the hexagon. These points were classified as apicomedial, i.e., relatively central to the hexagon, or as cortical, i.e., near the edges of the hexagon. Then a line was centered on each point. For points within the apicomedial region, the angular orientation was random. For points within the cortical region, the angular orientation was restricted to mostly parallel the edge, but with random variations within the restricted range. The cross-links (black dots) and myosin mini-filaments (blue barbells) were strategically placed in Panels a and b to illustrate cluster formation.

Figure 2. Characterizing oscillations. a) Phase portrait, which plots $r\bar{t_1}$ (contractility) versus $\frac{1}{\bar{\tau}(1+r)}$ (turnover). $\bar{t_1}$ and $\bar{\tau}$ are dimensionless versions of t_1 and τ (Appendix A). The bifurcation (sloped) line separates an upper region of oscillating solutions from a lower region of steady solutions. The two sets of oscillating solutions (circles, left set $\frac{1}{\bar{\tau}} = 0.5$, right set $\frac{1}{\bar{\tau}} = 1.0$) have the same color-coded offsets (0.01, 0.38, and 0.75) above the bifurcation line. Color-coded limit cycles for the b) left-set and c) right-set solutions from Panel a. Normalized deflections for the d) left-set and e) right-set solutions.

Figure 3. Switching from oscillations to ingression. a-d) Characterizing switching. Phase portrait (Panel a) including an initial oscillating solution (black) and four final steady solutions (green, purple, blue, and red). Time dependence of the duty ratio (Panel b). Panel c tracks the transition from the now unstable limit cycle (black) to the stable fixed point (initial locations of N and l on the limit cycle for clarity). Green solution exhibits critical slowing and has been truncated for clarity. Panel d plots the normalized deflection. e) Recapitulation of the experimental data (fitting parameters listed in Table 1). f) Magnification factor M.

Figure A1. Simulations of nonlinear dynamics, where the solutions are color-coded. a) Phase portrait, where $k_3 \frac{{l_o}^2}{k_1}$=15 ($k_3 \frac{{l_o}^2}{9k_1}$=15 for Figs. 2,3). The bifurcation line is solid, the threshold for numerical artifact is dashed. Phase plots in terms of b) normalized concentration $\frac{c}{c_o}$ and c) normalized number $\frac{N}{N_o}$. d-f) Corresponding time series. To facilitate comparison with reference *13*, these simulations are based on Eq. A5 with r set to 1, and Eq. A6 with r set to *0*.

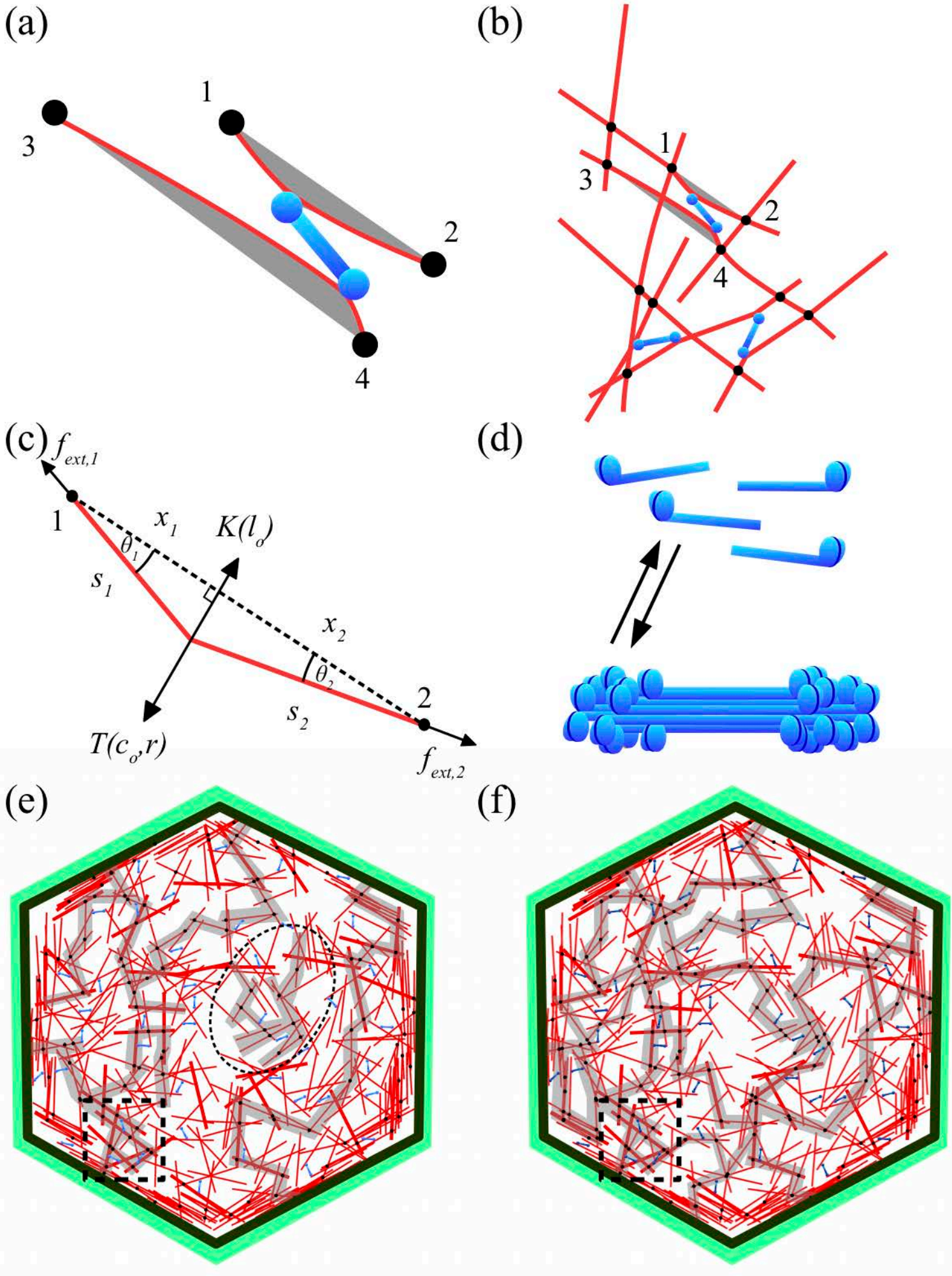
(a)
1
2
3
4
(b)
1
2
3
4
(c)
$f_{ext,1}$
1
x_1
$K(l_o)$
θ_1
s_1
x_2
θ_2
2
s_2
$T(c_o,r)$
$f_{ext,2}$
(d)
(e)
(f)

(a)

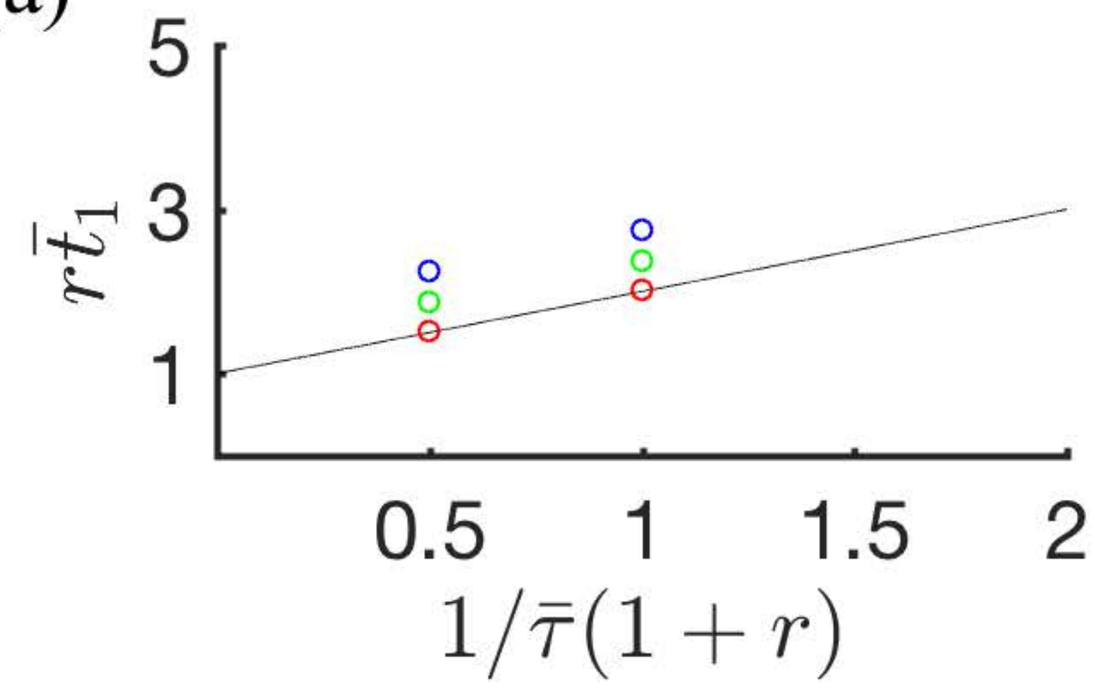
5
3
1
$r\bar{t}_1$
0.5
1
1.5
2
$1/\bar{\tau}(1+r)$

(b)

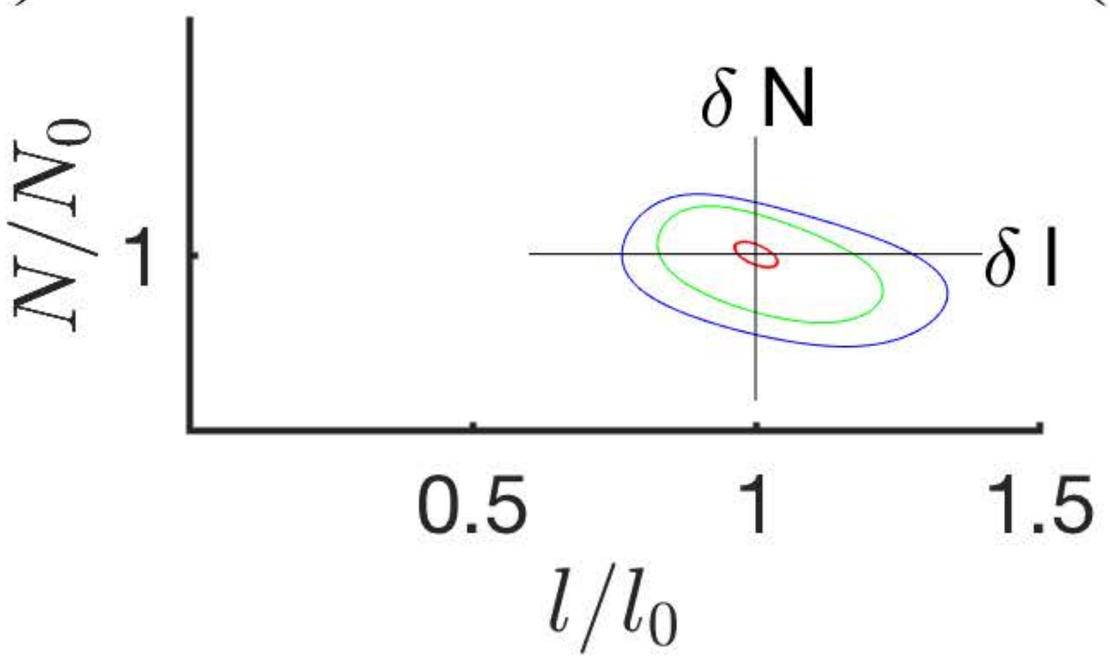
N/N_0
1
δ N
δ I
0.5
1
1.5
l/l_0

(c)

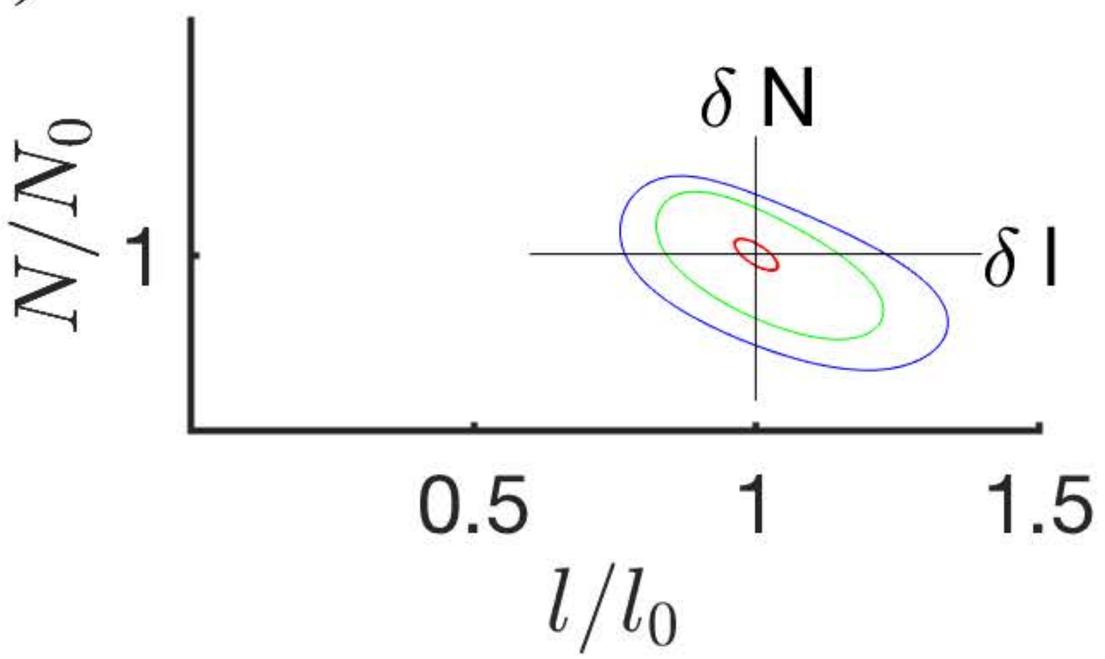
N/N_0
1
δ N
δ I
0.5
1
1.5
l/l_0

(d)

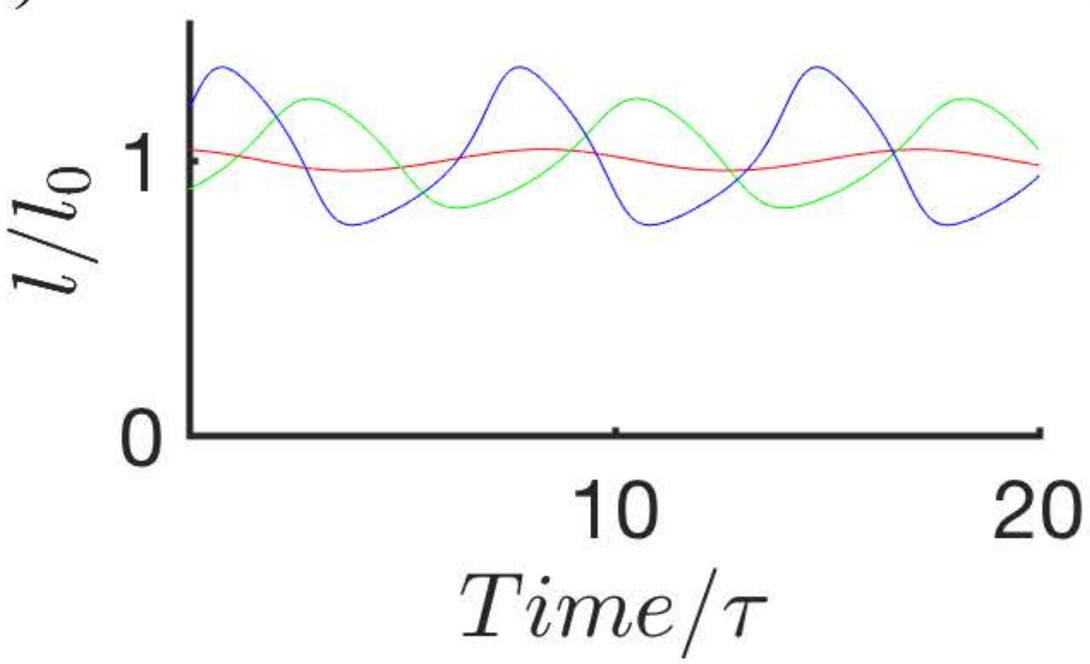
l/l_0
1
0
10
20
$Time/\tau$

(e)

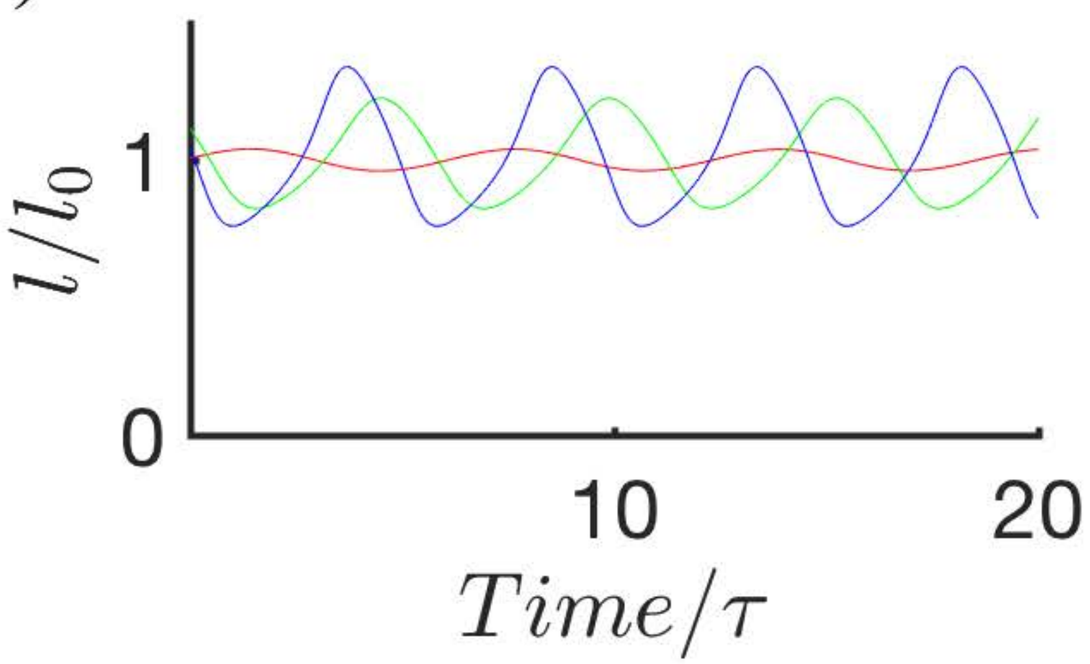
l/l_0
1
0
10
20
$Time/\tau$

(a)

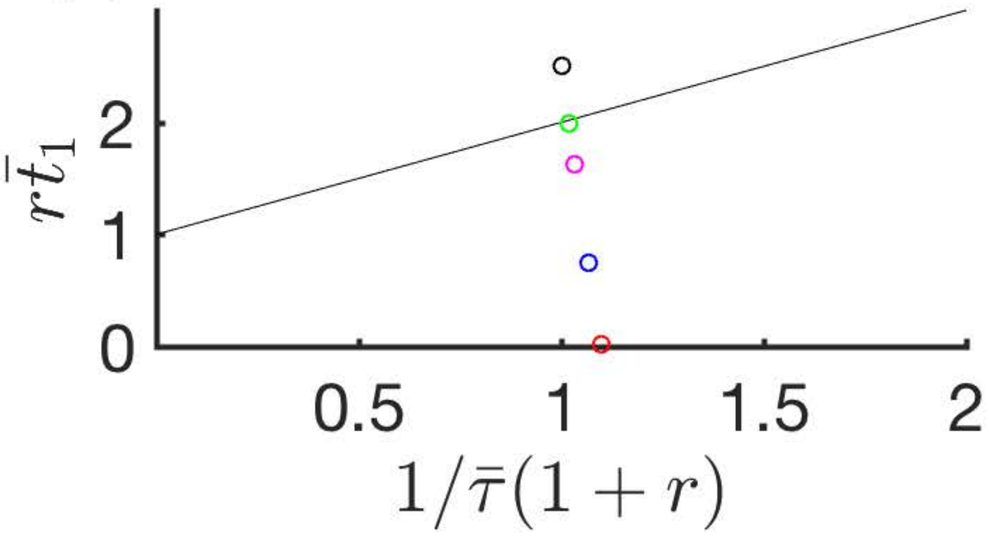
$r\bar{t}_1$
0
1
2
0.5
1
1.5
2
$1/\bar{\tau}(1+r)$

(b)

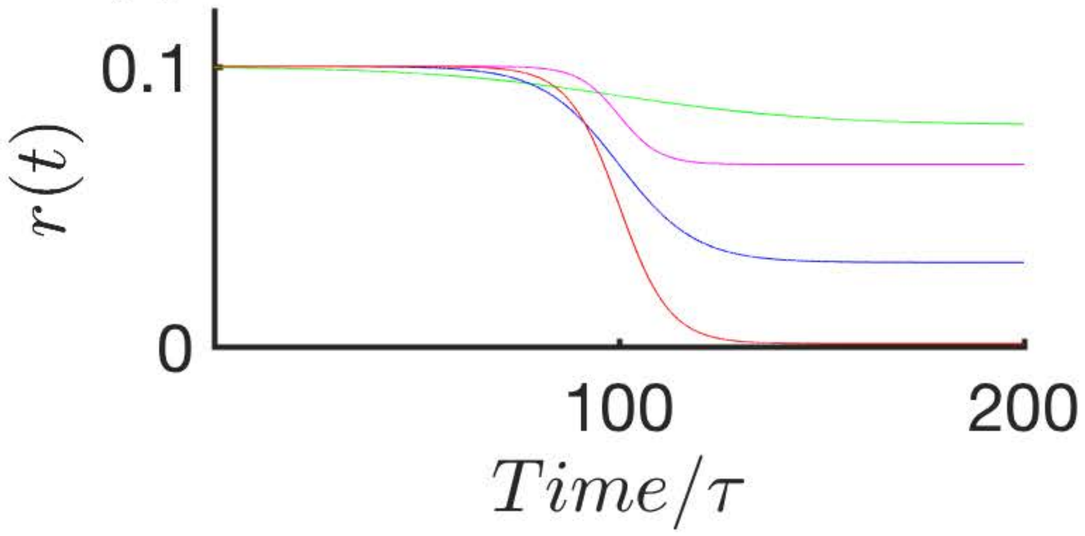
$r(t)$
0.1
0
100
200
$Time/\tau$

(c)

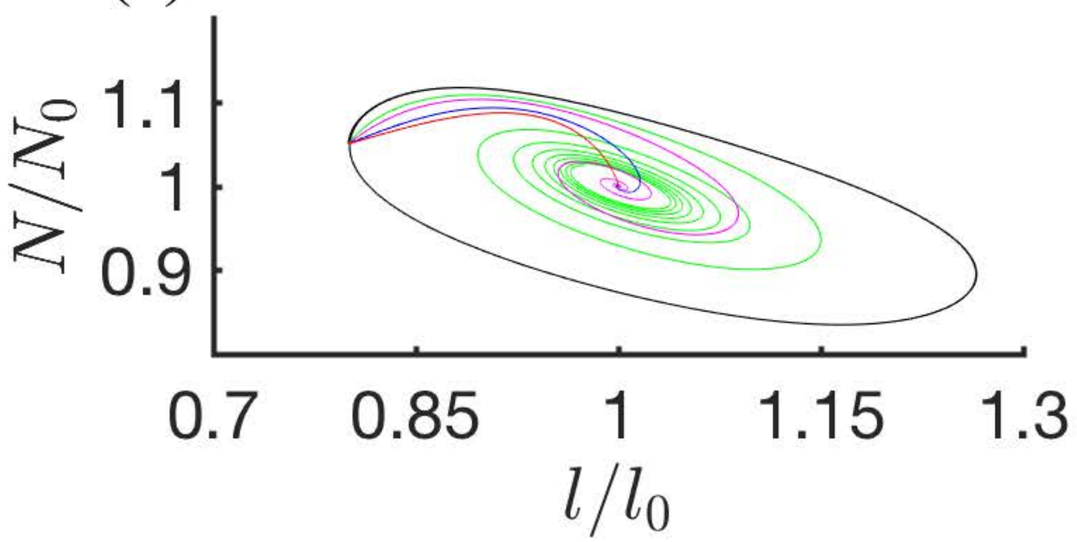
N/N_0
1.1
1
0.9
0.7
0.85
1
1.15
1.3
l/l_0

(d)

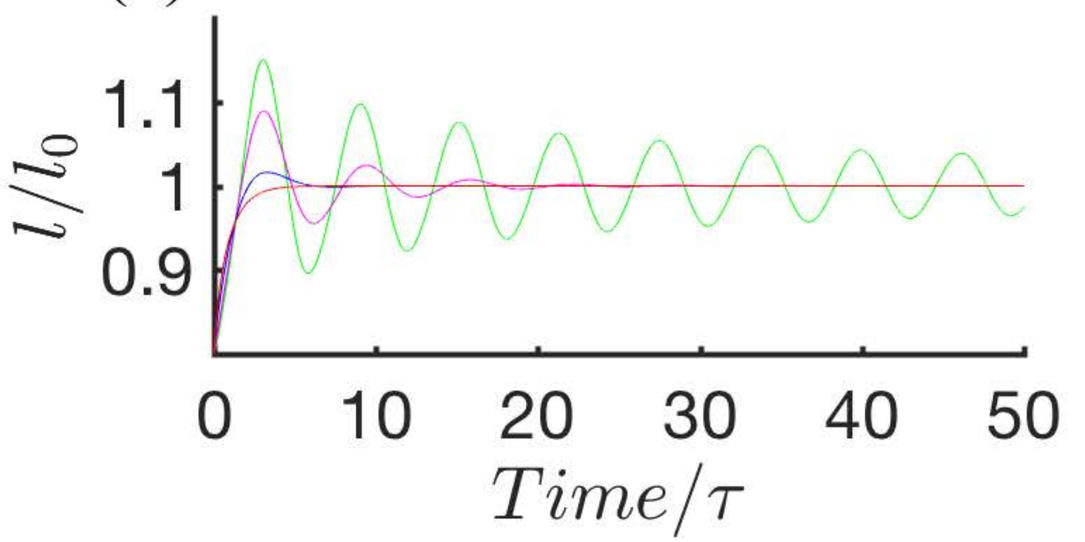
l/l_0
1.1
1
0.9
0
10
20
30
40
50
$Time/\tau$

(e)

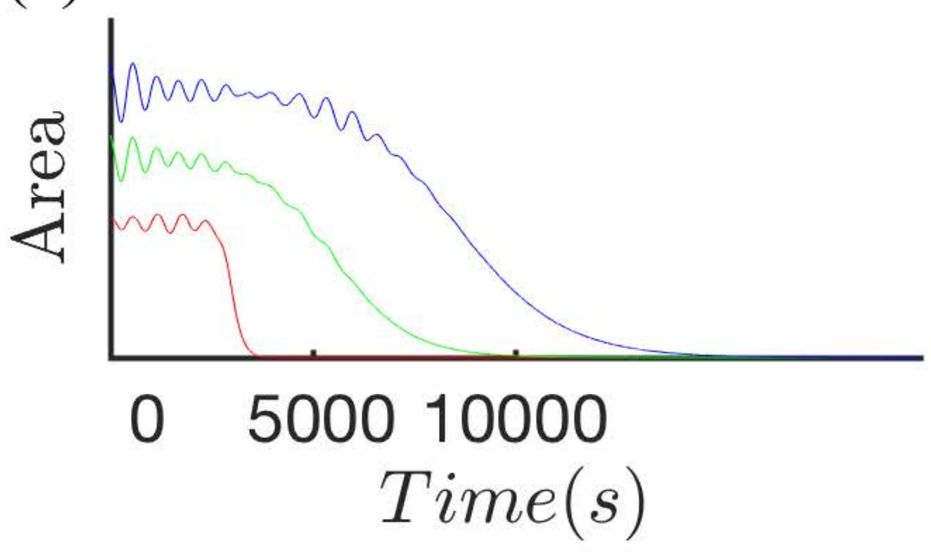
Area
0
5000
10000
$Time(s)$

(f)

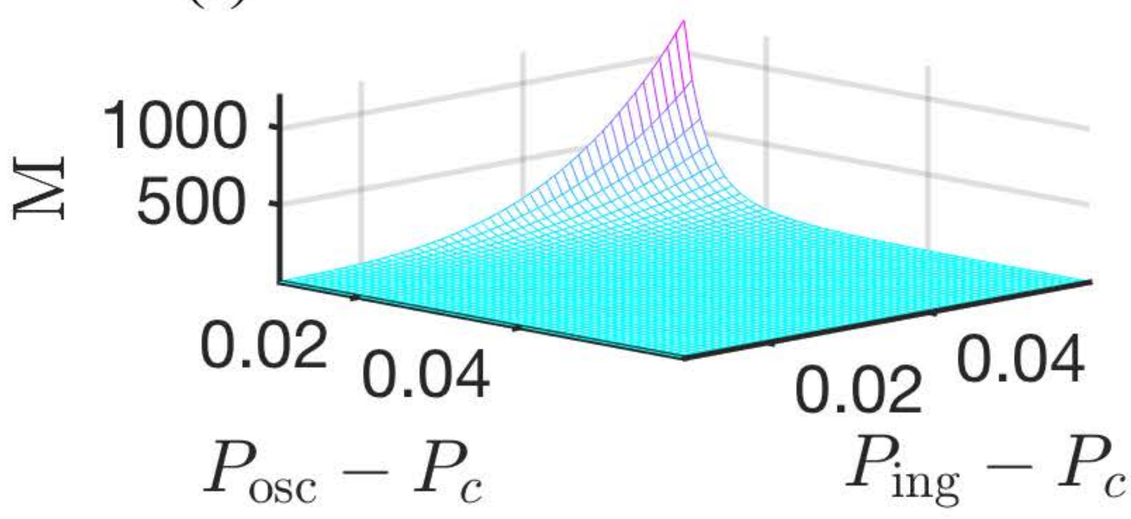
M
1000
500
0.02
0.04
$P_{\mathrm{osc}} - P_c$
0.02
0.04
$P_{\mathrm{ing}} - P_c$

(a)

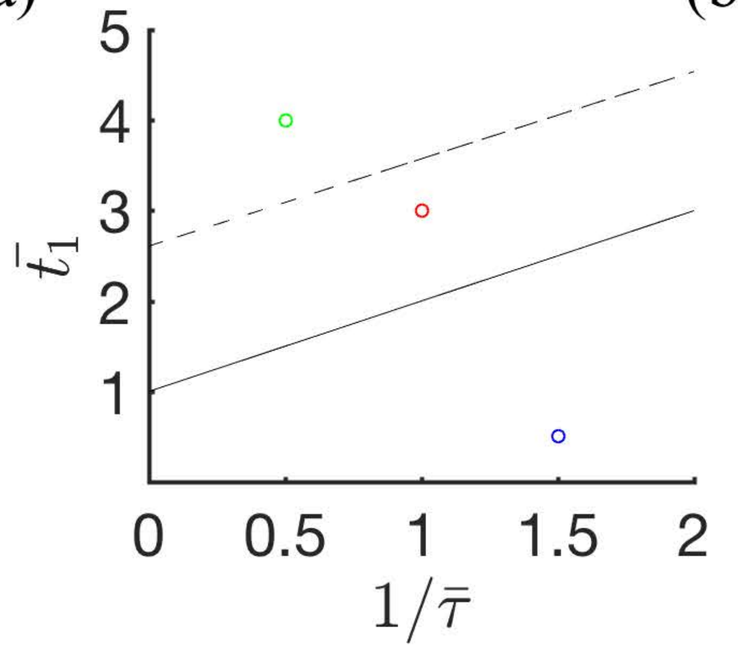
5
4
3
2
1
$\bar{t}_1$
0
0.5
1
1.5
2
$1/\bar{\tau}$

(b)

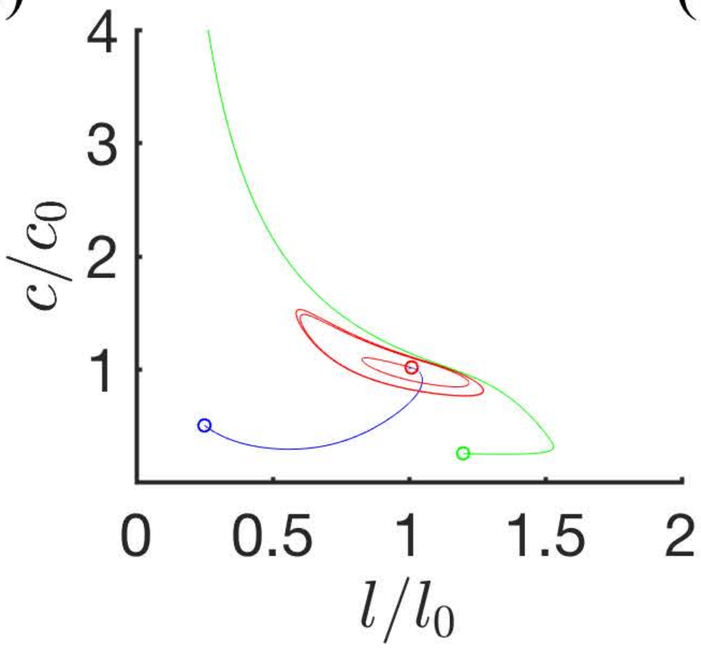
4
3
2
1
c/c_0
0
0.5
1
1.5
2
l/l_0

(c)

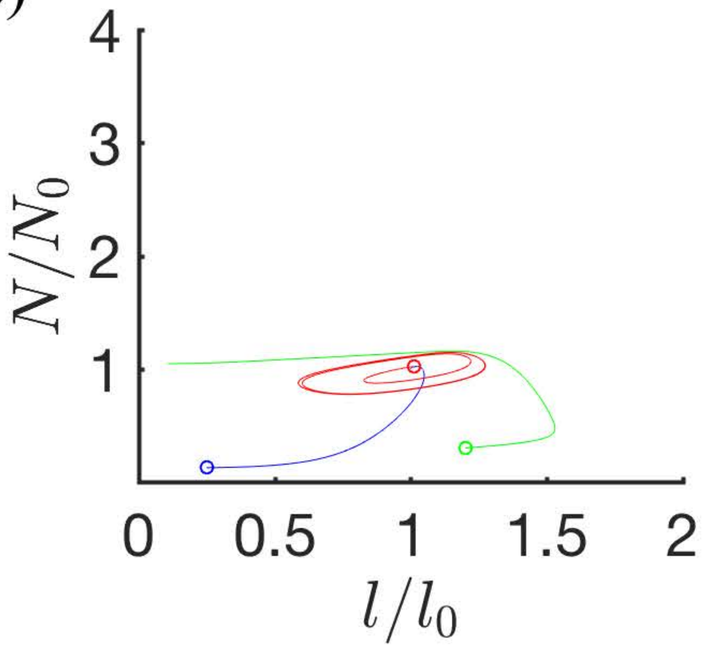
4
3
2
1
N/N_0
0
0.5
1
1.5
2
l/l_0

(d)

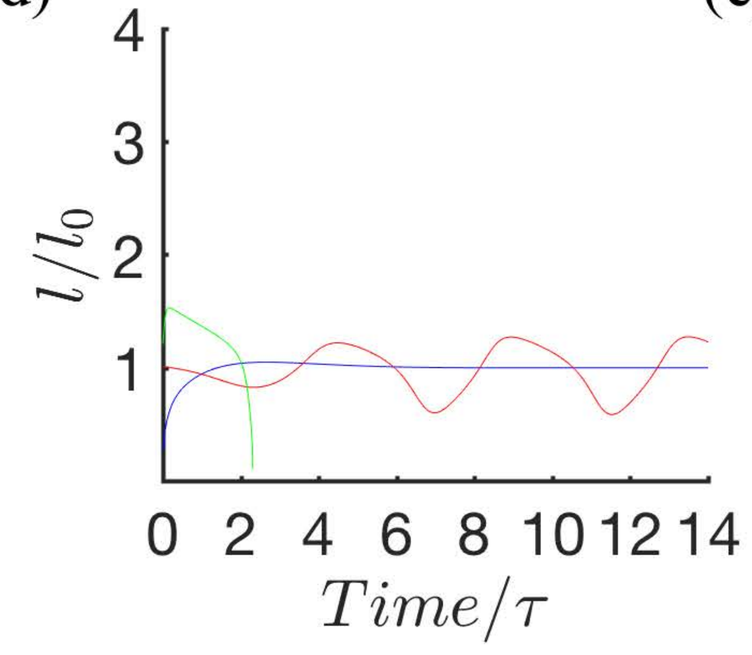
4
3
2
1
l/l_0
0
2
4
6
8
10
12
14
$Time/\tau$

(e)

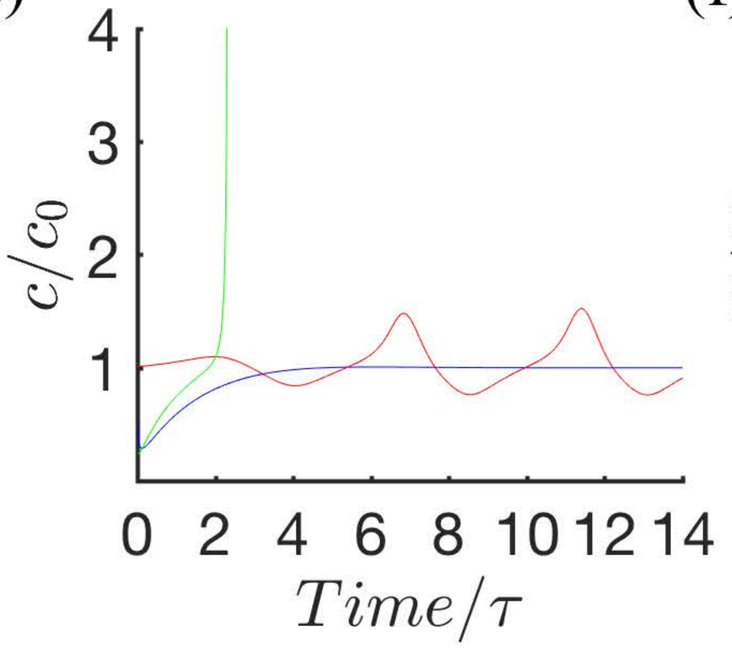
4
3
2
1
c/c_0
0
2
4
6
8
10
12
14
$Time/\tau$

(f)

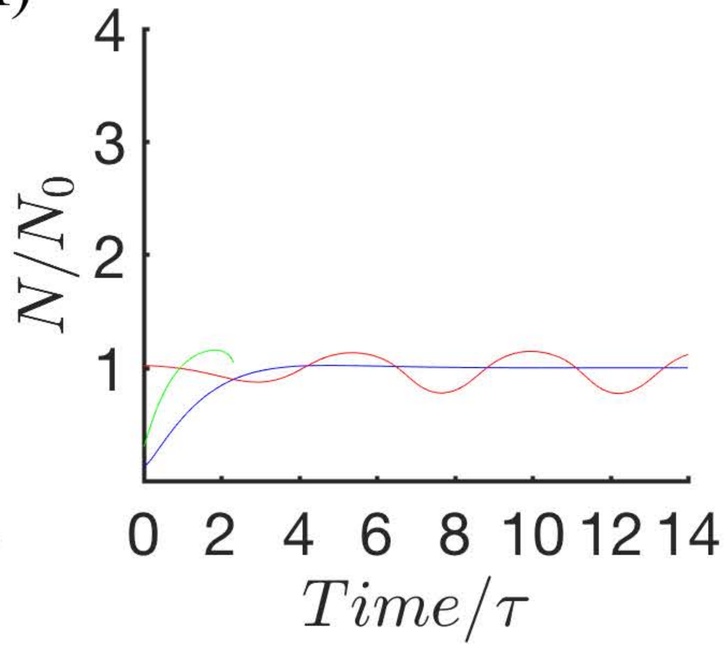
4
3
2
1
N/N_0
0
2
4
6
8
10
12
14
$Time/\tau$